Electron Bernstein Wave Studies: Current Drive; Emission and Absorption with Nonthermal Distributions; Delta-F Particle in Cell Simulations

R.W. Harvey[1], John R. Cary[2,6], G. Taylor[3], D.C. Barnes[2], T.S. Bigelow[4], S. Coda[5], J. Carlsson[6], J.B. Caughman[4], M.D. Carter[4], S. Diem[3], P.C. Efthimion[3], R.A. Ellis[3], N.M. Ershov[7], R.J. Fonck[8], E. Fredd[3], G.D. Garstka[8], J. Hosea[3], F. Jaeger[4], B. LeBlanc[3], B.T. Lewicki[8], C.K. Phillips[3], J. Preinhaelter[9], A.K. Ram[10], D.A. Rasmussen[4], A.P. Smirnov[7], J. Urban[9], J.B. Wilgen[4], J.R. Wilson[3], N. Xiang[2]
email: bobh@compxco.com

[1]CompX, Del Mar, CA 92014, USA; [2]CIPS, Univ. of Colorado, Boulder, CO 80309, USA; [3]PPPL, Princeton University, Princeton, NJ 08543, USA; [4]Oak Ridge National Laboratory, Oak Ridge, TN 37831, USA; [5]EPFL, CRPP, 1015 Lausanne, Switzerland; [6]Tech-X Corp., Boulder, CO 80303, USA ; [7]Moscow State University, Moscow, Russia; [8]University of Wisconsin, Madison, WI 53706, USA; [9]Czech Institute of Plasma Physics, Prague, Czech Republic; [10]PSFC, MIT, Boston, MA 02139, USA
e-mail contact of main author: bobh@compxco.com

Abstract. Electron Bernstein waves (EBW) are suitable for heating, current drive, and radiation temperature measurements of overdense plasma, $\omega_{pe}>>\omega_{ce}$, in spherical torus devices. In NSTX, design of a multi-megawatt EBW current drive system is supported by experimental measurements and computations of obliquely viewing, dual-polarization EBW emission (EBE) radiometry. Efficient EBW coupling, 80±20% at 16.5 GHz, is demonstrated, in agreement with calculations. Ohkawa EBWCD is calculated with Fokker-Planck and ray tracing codes to generate 40-50 kA/MW of off-axis current. Calculations for the Pegasus experiment are also presented. BXO emission from rf quasilinear modified nonthermal distributions calculated due to 1 MW of injected EBW power gives intermediate temperature between the thermal and tail nonthermal temperature. First results of slab-model simulation of EBW by a delta-f PIC code are given. Delta-f enables low-noise simulations of the linear mode-conversion of injected X-mode radiation to EBWs in the edge region of an overdense plasma, in good agreement with analytic analysis. At higher input power, harmonics of the fundamental EBW are nonlinearly generated, as well as decay into two EBWs at higher frequencies.

1. Introduction

The non-inductively sustained spherical torus (ST) is an attractive candidate for a high β fusion reactor. However, to stabilize the plasma some current may need to be driven off-axis by an external radiofrequency source. The "overdense" ($\omega_{pe}>>\omega_{ce}$) character of the ST precludes electron cyclotron current drive (ECCD) but allows electron Bernstein waves current drive (EBWCD). EBWs propagate in overdense plasma and strongly damp at EC resonances. EBW emission (EBE) diagnostics, ray-tracing, Fokker-Planck modeling, and particle simulation are being employed to study EBW coupling, propagation and CD physics in the NSTX[1], and Pegasus[2] STs. This research supports a long-term goal of enabling solenoid-free operation of NSTX plasmas at β > 20% by implementing a multi-megawatt EBWCD system using EBW coupling via oblique O-mode (O-X-B) launch and off-axis Ohkawa EBWCD in a region dominated by magnetically-trapped electrons [3].

2. Comparson of Theory and Experiment for NSTX and Pegasus

Figure 1(a) shows the characteristic electron resonance frequencies versus major radius (R) on the midplane of a β = 42% NSTX plasma. Mode conversion between EBWs and electromagnetic waves occurs near the upper hybrid resonance (UHR). EBWs propagating in from the UHR typically undergo a significant Doppler shift, reaching an $n_{\|} \geq 1$, and

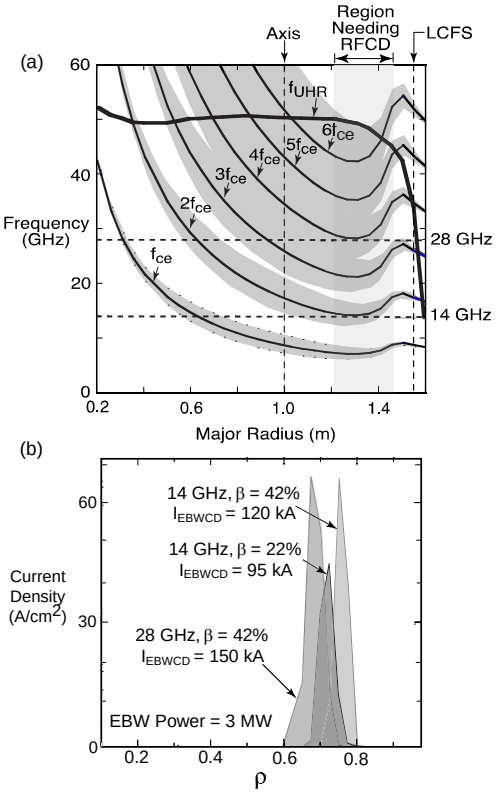

Fig. 1 (a) Characteristic frequency plot for β = 42% NSTX plasma. The plasma is overdense up to $6f_{ce}$. Shaded regions represent $n_{/} = \pm 1$ Doppler broadening of electron cyclotron resonances. Coupling to EBWs occurs near the UHR frequency (f_{UHR}). (b) Current density profile, calculated by CQL3D, plotted versus normalized minor radius, generated by 3 MW of EBW power at 14 GHz and 28 GHz for NSTX β = 22% and 42% plasmas. The vacuum toroidal field on axis is 0.35T.

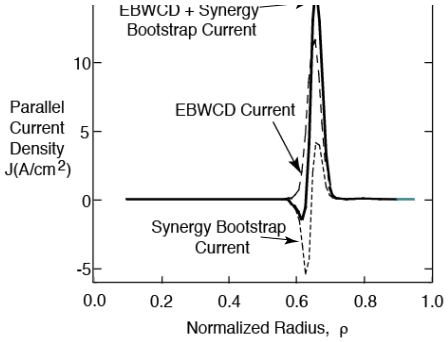

Fig. 2 EBWCD current density profile including bootstrap synergy for 1 MW of 28 GHz EBW power in a β =42% NSTX plasma.

consequently damp well before the non-Doppler shifted electron cyclotron resonance is reached. In order to non-inductively sustain NSTX plasmas at β > 20%, rf-driven current is needed in the region between R = 1.2 and 1.5 m, (normalized radius, ρ = 0.4 - 0.8). CQL3D [4] Fokker-Planck modeling of EBWCD at 14 and 28 GHz for β = 20 - 40% NSTX plasmas predicts that the EBW driven electron diffusion coefficient peaks near the trapped-passing boundary. As a result, a strong electron flux is driven from the population of transiting electrons having negative parallel velocity into the trapped region. This electron flux generates a negative Ohkawa current [5]. Current drive efficiencies of 40-50 kA/MW are predicted and the EBW-driven current density peaks between ρ = 0.6 and 0.8 (Fig. 1(b)), the region needed to support non-inductive operation of NSTX.

The normalized EBWCD efficiency, ζ_{ec} [6], is in the range 0.6 to 0.75, about twice the value obtained for ECCD in conventional large aspect ratio tokamaks. There is also a synergistic increase in bootstrap current due to enhanced EBW-induced pitch angle scattering that can significantly change the radial profile of the EBW-driven current (Fig. 2) [7].

B-X-O radiometry is employed on NSTX to evaluate the coupling efficiency of thermal EBE [8,9]. At fundamental EBW frequencies (8-18 GHz), the B-X-O coupling efficiency from L-mode plasmas has been measured to be ~ 80%, in good agreement with the 65% coupling efficiency predicted by a simulation that includes a 1-D full wave calculation of B-X-O coupling, antenna pattern modeling and 3-D EBW ray tracing (Fig. 3) [8]. The measured EBE polarization agrees with the elliptical polarization predicted by the simulation.

For EBE frequencies above fundamental, in H-mode plasmas, B-X-O coupling efficiency, measured by an 18-40 GHz quad-ridged antenna with limited local steering, was much lower than expected from modeling.

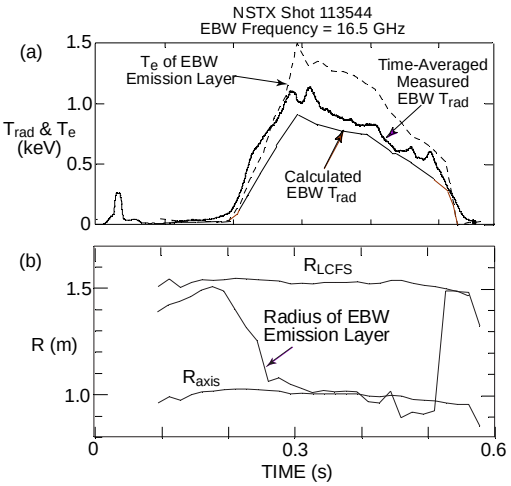

Fig. 3 (a) Measured 16.5 GHz EBE T_{rad} evolution (thick solid line) agrees well with calculated T_{rad} (thin solid line). EBW T_{rad} ~ 80% of T_e at emitting layer (dashed line) (b) Evolution of the radius of the EBW emission layer from the EBE simulation shows that 16.5 GHz EBE is from the axis from 0.25 to 0.5 s.

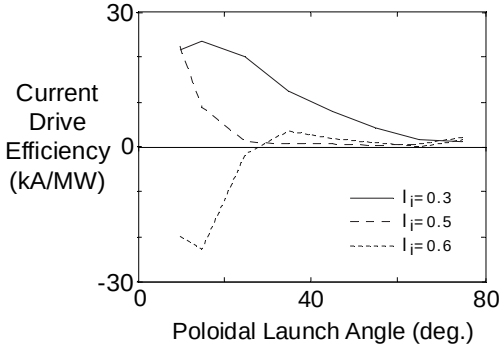

Fig. 5 Plot of EBWCD efficiency versus poloidal launch angle for Pegasus plasma cases with I_{tf} = 150 kA and various current profiles having l_i = 0.3, 0.5 and 0.6. The current drive direction may be sensitive to changes in the current profile shape.

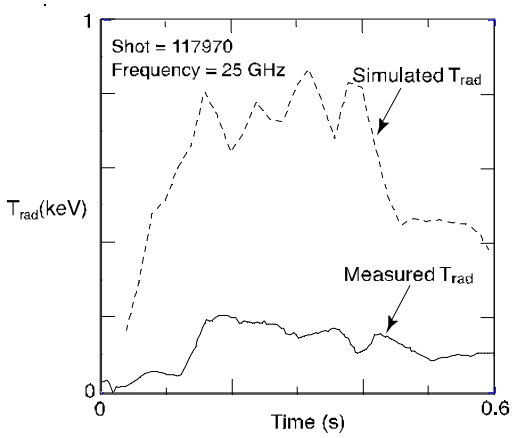

Fig. 4 Time evolution of the measured EBE T_{rad} at 25 GHz (solid line), compared to the simulated T_{rad} (dashed line) for NSTX shot 117970. Measured EBE polarization ($T_{//}/T_{\perp}$)

A comparison of measured and simulated 25 GHz EBE data is shown in Fig. 4. The measured EBE radiation temperature evolution (T_{rad}) (solid line) is about four times lower than the simulated T_{rad} (dashed line). Recent measurements with remotely steered 8-18 and 18-40 GHz B-X-O antennas [10] continue to show very low B-X-O coupling efficiencies in H-mode plasmas, even at fundamental EBW frequencies. There are several possible causes for the low B-X-O emission; EBW collisional loss due to low T_e at the UHR, local change in field pitch at the B-X-O conversion layer that is not included in the simulation and that is large enough to move the B-X-O emission window outside the antenna acceptance angle, or possibly an increase in edge bootstrap current density that blocks access to the core plasma, as has been speculated occur on MAST [11].

EBW heating and current drive experiments in the Pegasus ST, using up to 1 MW at 2.45 GHz [12], will investigate nonlinear edge effects, power deposition, and EBWCD. CQL3D Fokker-Planck modeling predicts an EBWCD of 20 - 40 kA/MW and an EBW-driven current density of up to 100 kA/cm^2 on axis. Under some conditions, the current direction is predicted to change with current profile shape (Fig. 4) and this will be investigated in the Pegasus experiments. Experiments will also combine HHFW heating with EBWCD. Demonstration of Ohkawa EBWCD in Pegasus will be important for validating predictions of the Fokker-Planck modeling and will provide critical data for implementing Ohkawa EBWCD on NSTX.

3. EBW Emission Due to Nonthermal Distributions in NSTX

GENRAY[13] is an all frequencies ray tracing code, including calculation of EBE from thermal or nonthermal distributions. Emission, j, and absorption, α, are calculated at each

point along rays originating at the detector, and the radiation transport equation for intensity I (per area-radian frequency-steradian), $n_r^2 \mathbf{s}.\nabla\left(n_r^{-2} I\right) = j - \alpha I$, is back-solved to the detector. Ray refractive index is n_r. Emission and absorption are calculated using a hot plasma dispersion relation[14] giving the wavenumbers and polarizations, along with a numerical, fully relativistic damping calculation. The BXO emission window is found with a shooting algorithm to obtain the central ray angles for a given receiver (antenna) position, giving 100% transmission[15].

Following, we show calculated EBE radiation temperature profiles for an NSTX experimental profile with thermal distributions, and compare to a case with EBWCD nonthermal distributions from a simulated OXB injection experiment. Both "low" and high beta cases are considered. We find that EBE, in conjunction with numerical calculations, provides a flexible means to diagnose thermal and nonthermal electron distributions.

3.1 Low-Beta Equilibrium

At low beta, curves of ω_{ce} vary approximately as inverse major radius, as distinct from Fig. 1, which has a magnetic well. We will focus on a range of frequencies between the first and second harmonic near the plasma edge, which are above the edge plasma frequency. The EBW rays from the detector--- along which radiation from within the plasma will travel back to the detector--- are launched with poloidal and toroidal angle such that the optimum parallel refractive index, $|n_{\|}| = \left(1 + \omega/\omega_{ce}\right)^{-1/2}$, obtained at the O-X mode conversion point where wave frequency, f, is equal to the plasma frequency, f_{pe}. We have chosen 16.5 GHz for this

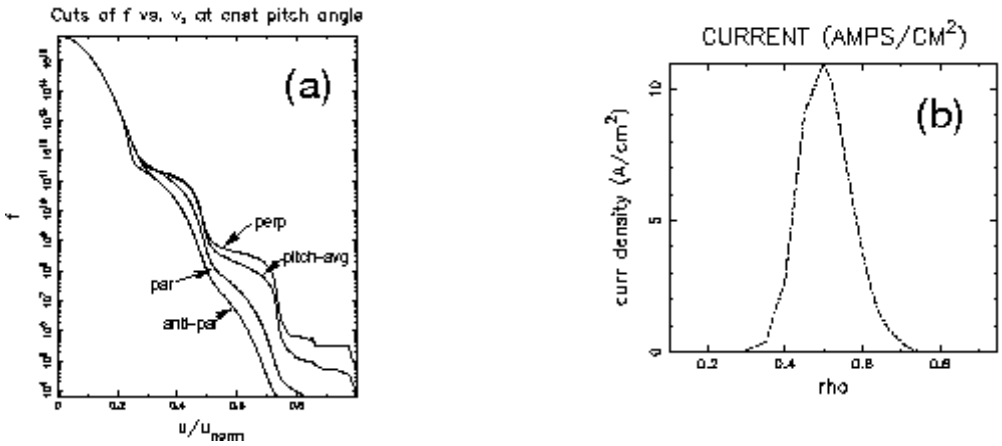

Fig. 6(a) Shows cuts through the electron distribution near the radius corresponding to the maximum EBW driven current. (b) Shows the driven current profile.

criterion, and launch the other frequencies at these angles. The loss of transmitted power at the neighboring frequencies remains small.

We use target nonthermal distributions as shown in Fig. 6. Figure 6(a) indicates the velocity distribution at a particular radius, calculated with the CQL3D Fokker-Planck[4]. The "staircase" effect in the tail of the distribution is due to the $J_1^2\left(k_\perp v_\perp / \Omega_c\right)$-variation of the quasi-linear diffusion coefficient. Figure 6(b) shows the current profile obtained from distributions calculated on the radial grid. The nonthermal electron tail current peaks at radius

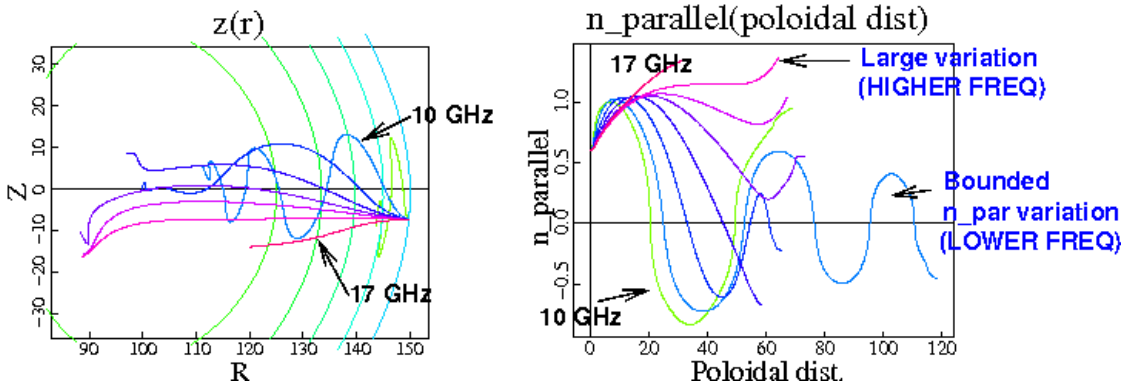

Fig. 7(a) Ray trajectories and (b) n_parallel versus poloidal distance along the trajectory, for an equispaced sequence of frequencies from 10 to 17 GHz.

0.5. These calculations are for OXB injection into shot 113544 plasma at frequency 16.5 GHz.

The EBW rays propagate towards the plasma center, but there is a marked difference between the lower frequencies with bounded $n_{\|} \le 0.5$-variation and the higher frequencies with secular variation to $n_{\|} \ge 1.0$ [Fig 7(a-b)]. The solution of the radiation transport equation for a low frequency range 10-12 GHz, and thermal plasma, then gives the results shown in Fig. 8(a) for the cumulative radiation intensity, I(R), flowing to the detector. Each of these curves arises from radiation near the first harmonic. The most remarkable feature is the

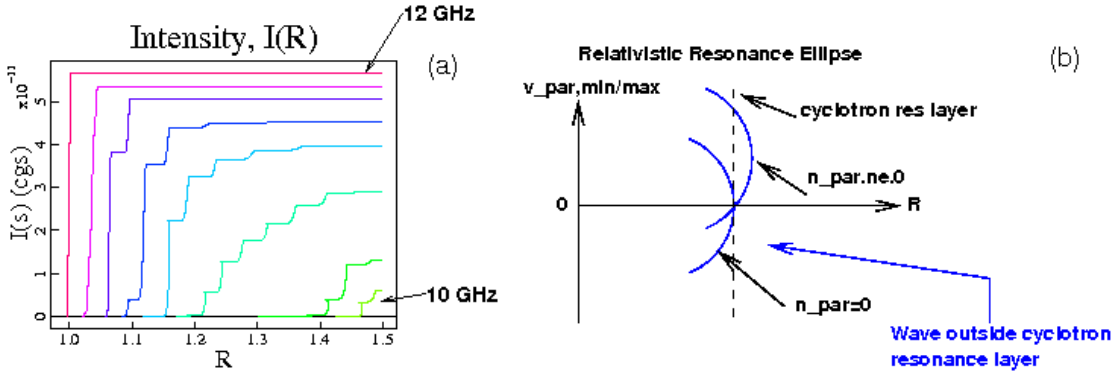

Fig. 8. (a) Cumulative emission intensity directed towards the detector, for frequencies in the range 10-12 GHz. (b) Parallel velocity range of the resonance ellipse versus major radius R.

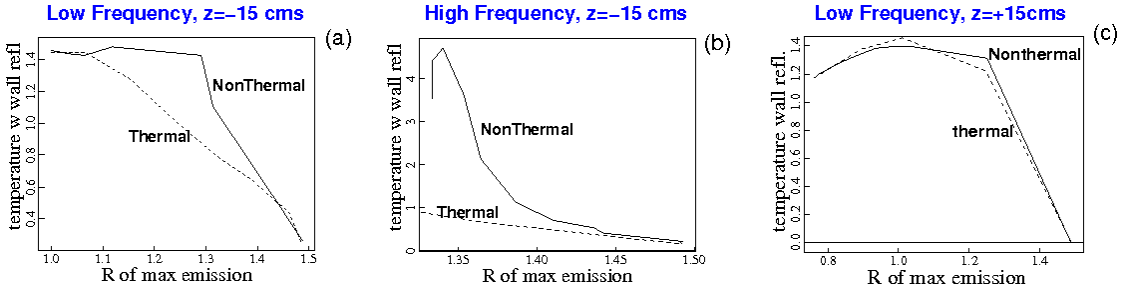

Fig. 9. Radiation temperature versus major radius R of maximum emission, for (a) Low frequency, z=-15 cms, (b) High frequency, z=-15 cms, and (c) Low frequency, z=+15cms

"staircase" effect in the radiation. This effect can be understood from Fig. 8(b), which schematically shows (as elaborated in Ref. 16) the $v_{\|}$-range of the relativistic resonance ellipse, accounting for the 1/R variation of the equilibrium magnetic field. For $n_{\|} = 0$, only electrons in the range $\left[v_{\|\min}, v_{\|\max}\right]$ and at major radius *inside* the cyclotron radius (the vertical

dashed line) can resonate with the wave. For $n_{\|} \neq 0$, Doppler-shifted resonance with electrons *outboard* of the cyclotron layer becomes possible. Thus, the staircase effect in Fig. 7(a) can be understood as due to the oscillation of $n_{\|}$ about a zero value, as shown for the low frequencies in Fig. 7(b). We expect this damping to be primarily on lower velocity electrons. Alternatively, the large $n_{\|}$ variation at high frequency leads to greater sensitivity to nonthermal electrons. These results are born out in Fig 9(a) and (b). Also, cursory examination of detector poloidal location reveals strong sensitivity, Fig. 9(c).

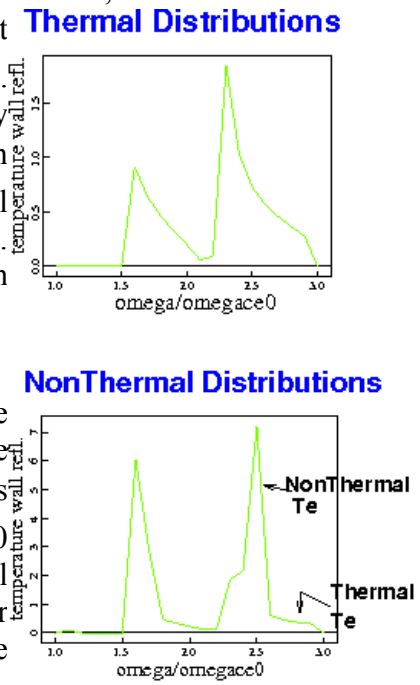

Fig. 10. Radiation temperature versus omega/Omega_ce, derived from (a) thermal, and (b) nonthermal distributions. High beta case.

3.2 High Beta Equilibrium

In high beta discharges such as in Fig.1, it is more difficult to achieve penetration of the EBW rays to the plasma center due to large $n_{\|}$-variation. Fig. 10 compares thermal and nonthermal distribution results for a 40 percent beta model NSTX equilibrium. The nonthermal component is similar to Fig. 6(a) but concentrated near radius ~0.7a. The thermal component is visible up outside the nonthermal layer, but is not visible inside of it.

Thus concerning the nontheral emission calculations, EBW emission provides a flexible measurement of thermal and nonthermal electron distributions over the range of beta in spherical tokamak experiments. Sensitivity to tail electrons necessitates an interplay between the experimental measurements and the modeling, to check that the physics of the experiment is well understood

4. Delta-f particle-in-cell Simulation of Mode Conversion to EBW

Full-wave modeling[17] has long been used for the computation of wave-plasma interactions in the interior of magnetically confined plasma. Plasma response is computed using a local linear conductivity. Thus, full-wave theory cannot include the effects of correlations over a full banana orbit, nor can it handle nonlinearities. To overcome these limitations, we are investigating the use of δf particle-in-cell (DFPIC) methods, which in principle should be able to handle all kinetic and nonlinear aspects, while having sufficiently low noise to study the physics of interest [18,19].

Due to their inherent statistical noise, regular (non δf) particle-in-cell (PIC) simulations of the coupling of radio-frequency power at realistic power levels are not practical for simulating linear EBW. Therefore, a noise-reduction δf algorithm has been implemented in VORPAL, a electromagnetic, massive parallel, hybrid plasma modeling code [20]. The implementation of the δf algorithm consists primarily of three parts: (1) particle loading, (2) particle pushing and weighting, and (3) field solving. For simplicity, we use a uniform particle loading.

The VORPAL δf simulations have allowed us to simulate the mode conversion between the extraordinary wave (X) and electron Bernstein wave (EBW) in both linear and nonlinear regimes. The amplitude of the incident wave can be as low as 10 V/m with only 144 particles per cell in a two-dimensional simulation. This wave amplitude is much smaller than typical values used in experiments, and well into the linear regime. Our simulations are two-

dimensional, with x the direction into the plasma, and y (the direction along the static magnetic field) being the second simulated direction. The non-simulated direction, z, is the vertical direction, equivalent to the poloidal direction in toroidal geometry.

4.1 Simulation results in linear regime

Our simulation model has been verified in several ways. We found agreement in comparisons with available linear dispersion theory. We next considered the regime of 100% X-B mode conversion found by Ram *et al* [21]. That theory relies on a gyroradius expansion that requires the incident frequency to be less than twice the electron gyrofrequency. In this regime, we verified that 100% mode conversion can occur [Fig. 11].

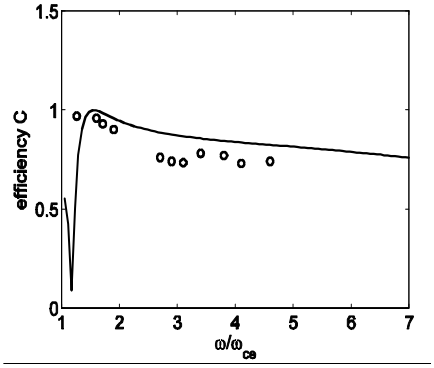

Fig. 11. X-B conversion efficiencies versus frequency from the simulations (solid line), and theory (circle).

Because the theory of Ram *et al* is valid only for frequencies less than twice the electron gyrofrequency, a question is whether 100% mode conversion can be found in other frequency ranges, namely drive frequency twice or more the electron gyrofrequency, where expansion in the gyroradius does not apply. Our DFPIC simulations show this is not the case. This is due to the fact that as the driving frequency increases, the cutoffs of the X wave will move closer to the upper hybrid resonance (UHR), which causes insufficient room for the phase accumulation needed in the cutoff-resonance-cutoff triplet mechanism for 100% mode conversion.

4.2 Simulation results in nonlinear regime

Our use of DFPIC has further enabled us to study nonlinear wave coupling effects [22] and, in fact, discover an unusual form of mode-mode coupling where the pump wave can interact with itself and produce a wave at the second harmonic. Typically, mode-mode interactions must involve three waves to satisfy the resonance condition, unless the dispersion relation is linear, as seen by by Mix et al [23]. Here, even though the EBW dispersion relation is nonlinear, a strong production of energy at the second harmonic can occur.

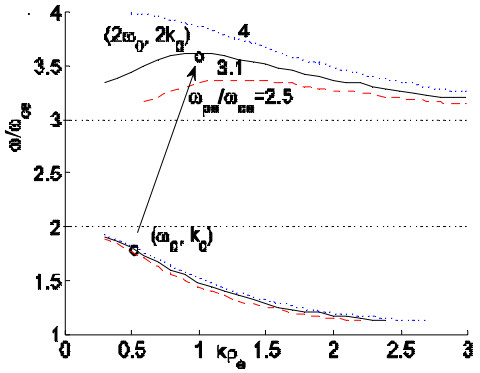

Fig. 12. EBW dispersion relation for various values of ω_{pe}/ω_{ce}.

The key to second-harmonic mode generation can be seen in Fig. 12. This figure shows the EBW dispersion relations at fixed density and magnetic field, for various values of ω_{pe}/ω_{ce}. We consider lines of constant slope, radiating from the origin, and their intersections (k_l, ω_l) with the lower curve and (k_u, ω_u) with the upper curve. Because these intersections are on a line, we know that $\omega_u/\omega_l = k_u/k_l$. For infinite slope, Fig. 12 shows that the ratio of frequencies and wavenumbers is < 2, while as the slope is reduced towards zero, the ratio asymptotes to 3. Therefore, at some intermediate point the slope is exactly 2. At that point, resonant production of second-harmonic modes can occur giving significant transfer of energy to the second harmonic, and leading to energy deposition elsewhere.

Figure 12 shows the possibility of a very strong interaction as well. The arrow points to a case where the second-harmonic mode has zero group velocity. In this case, the second harmonic energy propagates only very slowly, if at all, away from the interaction point.

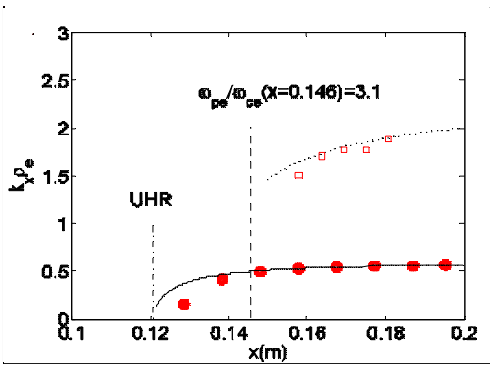

Φιγ. 13. Χομπαρισον οφ τηε δισπερσιον χυρ ϖεσ φροµ δφ simulation (circle and square) and theory (dotted line for the 2nd harmonic and solid line for the fundamental mode).

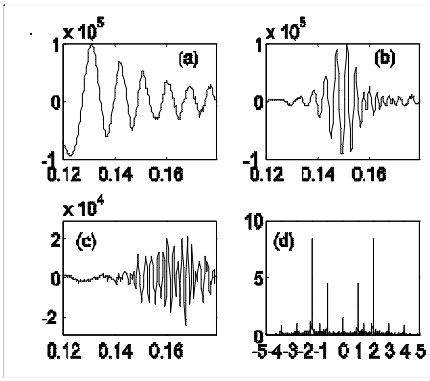

Fig. 14. Ex from the full PIC simulation with (a) fundamental (b) 2nd and (d) 3rd harmonic modes. The power spectrum of Ex at x = 0.15m is shown in (d).

We have confirmed harmonic generation through our DFPIC simulations. The phase-space (k_x-x) diagram for our simulated case is shown in Fig. 13. Local fourier transforms show that our simulations are correctly propagating the EBW modes. Harmonic generation is also confirmed by our simulations, as shown in Fig. 14. Fig. 14(a), (b) and (c) show the full PIC simulation of the spatial distribution of the electrostatic field at fundamental, second and third harmonics for $E_0 = 10^5$ V/m at $t = 630/\omega$. In this case the interaction is sufficiently strong that the amplitude of the second harmonic mode is comparable to that of the fundamental. The spectrum of the electrostatic field at x = 0.15m is presented in Fig. 14(d), and it clearly shows the higher harmonic generation. However, the third harmonic, which is not resonantly generated, is of lower amplitude.

This research was supported U.S. Dept. of Energy contracts DE-AC02-76CH03073, DE-FG02-96ER54375 and DE-FG03-02ER54684.

[1] M. Ono, *et al.*, Proc. 17th IAEA Fus. Energy Conf. (IAEA, Vienna,1999), Vol.3, p. 1135
[2] G. D. Garstka, *et al.*, *Phys. Plasmas* **10**, 1705 (2003)
[3] G. Taylor, *et al.*, AIP Conf. Proc. **787**, 337 (2005)
[4] R.W. Harvey and M.G. McCoy, Proc. IAEA TCM, Advances in Sim. and Modeling of Thermo-nuclear Plasma, Montreal, (IAEA, Vienna, 1993), p. 489; USDOC NTIS Doc. No. DE93002962
[5] G. Taylor, *et al.*, *Phys. Plasmas* **11**, 4733 (2004)
[6] T.C. Luce, *et al.*, Phys. Rev. Lett. **83**, 4450 (1999)
[7] R. W. Harvey and G. Taylor, *Phys. Plasmas* **12**, 051509 (2005)
[8] J. Preinhaelter, *et al.*, AIP Conf. Proc. **787**, 349 (2005)
[9] G. Taylor, *et al.*, *Phys. Plasmas* **12**, 052511 (2005)
[10] S. J. Diem, *et al*, *"T_e(R,t) Measurements using Electron Bernstein Wave Thermal Emission on NSTX"* to be published in Rev. Sci. Instrum. (2006)
[11] V. Shevchenko, *et al.* Proc. EC13 Conference, Nizhny Novgorod, Russia (2004), p. 162
[12] G. D. Garstka, *et al.*, Nucl. Fusion **46,** S603 (2006)
[13] A.P.Smirnov, R.W.Harvey, E.Nelson-Melby, A.K. Ram, EC14 Conf., Santorini, (2006)
[14] C.B. Forest, P.K. Chattopadhay, R.W.Harvey, A.P. Smirnov, Phys. Pl. **7,** 1352 (2000).
[15] V. Kopechy, J. Preinhaelter, J. Vaclavik, *J. Plasma Phys.,* 3, 179, (1969).
[16] R.W. Harvey, M.G. McCoy and G.D. Kerbel, Phys.Rev.Lett. **62**, 426 (1989)
[17] E. F. Jaeger, *et al.*, Phys. Plasma 9, 1873 (2002).
[18] S. E. Parker and W. W. Lee, Phys. Fluids B 5, 77(1992).
[19] G. Hu and J. A. Krommes, Phys. Plasmas 1, 863 (1994).
[20] C. Nieter and J. R. Cary, J. Comput. Phys. 196, 448 (2004).
[21] A. K. Ram and S. D. Schultz, Phys. Plasmas **7**, 4084 (2000).
[22] M. Porkolab and R. P. H. Chang, Rev. Mod. Phys. 50, 745 (1978).
[23] J. L. P. Mix, L. N. Litzenberge, and G. Berkefi, Phys. Fluids 15, 2020 (1972).